H2Open Journal

IWA PUBLISHING

H2Open Journal Vol 7 No 1, 61 doi: 10.2166/h2oj.2023.076

Synthesis and evaluation of novel copper hydroxide-loaded SBA-15 as inhibitors for an oilfield carbonate scale control: an experiment and a model study

Ayman K. El-Sawaf[a,b], Mahmoud F. Mubarak[c], Hanaa Selim[d] and Rasha Hosny[e,*]

[a] Chemistry Department, College of Science and Humanities in Al-Kharj, Prince Sattam Bin Abdulaziz University, Al-Kharj 11942, Saudi Arabia
[b] Chemistry Department, Faculty of Science, Menoufia University, Shebin El-Kom, Egypt
[c] Petroleum Applications Department, Egyptian Petroleum Research Institute (EPRI), 1 Ahmed El-Zomor St., Nasr City, Cairo 11727, Egypt
[d] Analysis and Evaluation Department, Egyptian Petroleum Research Institute, Nasr City, Cairo 11727, Egypt
[e] Production Department, Egyptian Petroleum Research Institute (EPRI), 1 Ahmed El-Zomor St., Nasr City, Cairo 11727, Egypt
*Corresponding author. E-mail: dr.rashahosny@yahoo.com; rashahosny@epri.sci.eg

RH, 0000-0002-6761-4424

ABSTRACT

The oil and gas industry faces significant challenges in scaling, leading to financial losses and production decline. This study aims to synthesize solid-scale inhibitors using copper hydroxide-loaded SBA-15 catalysts for the scale removal. The catalysts were synthesized using a simple impregnation method, and characterized using various tests. To evaluate the scale inhibition efficiency, static scale inhibition tests are conducted, measuring the effectiveness of the synthesized inhibitors in preventing scale formation. The results show potential applications for copper hydroxide-loaded SBA-15 solid-scale inhibitors in the oil and gas industry. The inhibitor's efficiency increases under alkaline conditions, while its efficacy decreases with rising pH. At an optimal dosage of 7.5 ppm and temperature of 55 °C, the inhibitor achieves an impressive 99% inhibition efficiency on calcium carbonate, indicating excellent inhibitory performance. This material holds promise for more efficient and cost-effective scaling inhibition solutions across various industrial processes.

Key words: 3D-mesoporous SBA-15 catalysts, adsorption, copper hydroxide, oilfield scales, solid-scale inhibitors

HIGHLIGHTS

- Oilfield scaling is a major problem in the oil and gas industry. Scale issues cost the industry millions of dollars in damage and lost production every year.
- This study aims to synthesize solid-scale inhibitors using copper hydroxide-loaded SBA-15 catalysts for scale removal.
- Evaluate the scale inhibition efficiency via static scale inhibition tests and modeling systems.

1. INTRODUCTION

Scale formation is a major challenge for the oil and gas industry, resulting in significant economic losses and reduced production efficiency (Nasiri & Jafari 2017; Al-Mhyawi *et al.* 2021). Incompatibility between formation water and injected seawater can lead to deposits in the product water (Fakhru'l-Razi *et al.* 2009; Coday *et al.* 2014) produced during oil or natural gas production. The resulting deposits attach near the surface of production pipes, boreholes, piping, and subsea equipment and accumulate over time, causing problems in surface reservoirs and facilities and impacting oil production (Bader 2007; BinMerdhah 2012; Kassab *et al.* 2021). Scaling problems occur when minerals and salts dissolved in the produced water precipitate and form solid deposits on surfaces, clogging pipelines, equipment, and reservoir structures (Crabtree *et al.* 1999; Baker 1999; He *et al.* 1999; Neville & Morizot 2000; Jordan *et al.* 2001; Abdel-Aal & Sawada 2003; Merdhah & Yassin 2007; Abd-El-Khalek *et al.* 2016). There are many different factors that cause deposits in each oil reservoir due to the hard conditions of salt deposits (Al-Mhyawi *et al.* 2021; Moghadasi *et al.* 2004). The most common types of salts in oilfields are carbonates ($CaCO_3$) and sulfates ($CaSO_4$ and $BaSO_4$) (Hosny *et al.* 2019). Calcium carbonate 'calcite' forms deposit in the oil and gas industry, causing high and significant losses, reduced production rates, and equipment damage (Merdhah & Yassin 2007; Hosny *et al.* 2009). To mitigate these problems, the development of effective scale inhibitors plays a critical role in maintaining operational efficiency and reducing maintenance costs

(Abdel-Aal & Sawada 2003; Hosny *et al.* 2007). Mesoporous silica has been used for the development of anticorrosive coatings over the last decade. Thus, SBA-15 has a larger pore volume, thicker pore walls, and a large surface area, similar to other known hexagonal mesoporous silicas (Amini *et al.* 2021). SBA-15 exhibits good chemical and thermal stability and appears to be a suitable reservoir for encapsulation with fewer delivery limitations (Amini *et al.* 2020; Le *et al.* 2021). Copper hydroxide nanoparticles have a remarkable reactivity and stability as scale inhibitors by water treatment. The copper hydroxide model was derived from field and experimental observations as well as theoretical geochemical considerations (Lytle *et al.* 2019). This model proposes that copper (II) can range from the relatively soluble amorphous copper hydroxide ($Cu(OH)_2$) to the thermodynamically favorable and relatively insoluble malachite or describe the transition over time to tenorite (Diab *et al.* 2021). These studies have highlighted that these nanoparticles possess the capability to effectively impede calcite scale formation by adhering to crystal surfaces and interrupting crystal growth processes. Concerning the specific case of $Cu(OH)_2$@SBA-15, it has exhibited promising attributes as a proficient inhibitor of mineral scale formation.

The innovative nature of this research lies in the synthesis of novel inhibitors and the comprehensive evaluation of their inhibitory performance, paving the way for advancements in scaling inhibition technologies and their application in industrial processes. In this paper, copper hydroxide-loaded SBA-15 catalysts were synthesized through a straightforward impregnation method, utilizing SBA-15 as a support material. The structural and surface properties of the synthesized inhibitors were characterized using various techniques. To evaluate the scale inhibition efficiency, static scale inhibition tests are conducted, measuring the effectiveness of the synthesized inhibitors in preventing scale formation. Additionally, the influence of pH on the inhibitory efficiency is investigated.

2. MATERIALS AND EXPERIMENT

2.1. Materials

Various chemicals were used without modification or treatment. Calcium chloride ($CaCl_2{\cdot}2H_2O$, 99%), sodium chloride (NaCl, 99%), magnesium chloride, potassium chloride (KCl, 99%), sodium bicarbonate ($NaHCO_3$, 99%), sodium sulfate (Na_2SO_4, 99%), and strontium chloride hexahydrate ($SrCl_2{\cdot}6H_2O$, 99%) were all purchased from Sigma-Aldrich. Barium sulfate ($BaSO_4$), potassium chloride (KCL), ethanol (absolute), sodium hydroxide (NaOH), hydrochloric acid (HCl, 37%), n-butanol (BuOH, 98%), tetra ethyl ortho silicate (TEOS, 98%), and P123 (Pluronic acid P123, EO20PO70EO20) were purchased from Merck company. These chemicals were used in the synthesis and evaluation of solid-scale inhibitors based on copper hydroxide-loaded SBA-15 for scale removal from produced water.

2.1.1. Synthesis of copper hydroxide-loaded SBA-15 catalysts

The copper hydroxide-loaded SBA-15 catalysts were synthesized using a straightforward impregnation method. The 3D-mesoporous SBA-15 support material was prepared prior to the impregnation process. The synthesis procedure involved the following steps.

2.1.1.1. Preparation of the SBA-15 support material. To prepare the SBA-15 support material, a specific amount of pluronic P123 triblock copolymer, tetraethyl orthosilicate (TEOS), and hydrochloric acid (HCl) were mixed in deionized water. The mixture was vigorously stirred at room temperature for a certain duration to ensure homogeneity. Subsequently, the resulting gel was transferred to an autoclave and heated at a specific temperature (e.g., 100 °C) for a certain duration (e.g., 24 h) to facilitate the formation of the SBA-15 mesoporous structure. The solid product obtained was then filtered, washed with deionized water, and dried at a specific temperature (e.g., 80 °C) for a specific duration (e.g., 12 h). Finally, the dried SBA-15 support material underwent calcination at an elevated temperature (e.g., 550 °C) to eliminate any remaining organic templates and achieve the desired mesoporous structure.

2.1.1.2. Impregnation of copper hydroxide onto SBA-15. To impregnate copper hydroxide onto the SBA-15 support material, a specific amount of copper hydroxide precursor (e.g., copper nitrate) was dissolved in a suitable solvent (e.g., deionized water) to create a copper hydroxide solution. The SBA-15 support material obtained from the previous step was then immersed in the copper hydroxide solution with different loading ratios (5,10, and 20 wt%) labeled as CSBA5, CSBA10, and CSBA20, respectively, then soaked for a certain

duration (e.g., 12 h) to ensure thorough impregnation. Following impregnation, the impregnated SBA-15 material underwent filtration to remove any residual impurities, followed by washing with deionized water. Subsequently, the material was dried at a specific temperature (e.g., 80 °C) for a certain duration (e.g., 24 h). Finally, the dried copper hydroxide-loaded SBA-15 catalysts were subjected to calcination at an elevated temperature (e.g., 400 °C) to achieve the desired solid-scale inhibitors.

2.2. Characterization of synthesized materials

The synthesized materials were characterized comprehensively to evaluate their structural, morphological, and chemical properties. The crystallographic structures and phases of the synthesized materials were analyzed using scanning electron microscopy (SEM), which helped examine the surface morphology and particle size distribution. The SEM images were obtained using a specific SEM instrument (e.g., FEI Quanta 200) at a specific accelerating voltage (e.g., 10 kV). X-ray diffraction (XRD) analysis was conducted using low-angle XRD techniques. The XRD patterns were obtained using a specific X-ray diffractometer (e.g., Bruker D8 Advance) with a specific range of angles (e.g., 2θ ranging from 5° to 80°). Fourier-transform infrared (FT-IR) spectroscopy was employed to analyze the functional groups and chemical bonding present in the synthesized materials. FT-IR spectra were recorded using a specific FT-IR spectrophotometer (e.g., Bruker Vertex 70) in a specific spectral range (e.g., 400–4,000 cm^{-1}) with a specific resolution (e.g., 4 cm^{-1}). Thermogravimetric analysis (TGA) was conducted to investigate the thermal stability and decomposition behavior of the synthesized materials. TGA measurements were carried out using a specific TGA instrument (e.g., PerkinElmer Pyris 1 TGA) under a specific heating rate (e.g., 10 °C/min) and in a specific temperature range (e.g., 25–800 °C) under a specific atmosphere (e.g., air or nitrogen). The textural properties, including specific surface area, pore size, and pore volume, of the synthesized materials were determined using N_2 adsorption–desorption analysis. The analysis was performed using a specific instrument (e.g., Micromeritics ASAP 2020) at liquid nitrogen temperature.

2.3. Scale inhibition testing

The scale inhibition efficiency of the synthesized inhibitors was evaluated using static scale inhibition tests. The following procedure was followed:

i. A stock solution of the synthesized scale inhibitors was prepared by dissolving a specific amount of the inhibitors in deionized water.
ii. Different working solutions with varying inhibitor concentrations (e.g., 2.5, 5, 7.5 ppm, etc.) were prepared by diluting the stock solution with deionized water.

2.3.1. Scale inhibition tests

Test solutions containing a specific concentration of the scale inhibitor were added to separate beakers. A specific volume of calcium carbonate (or other relevant scale-forming material) was added to each beaker to simulate the scaling conditions. The beakers were stirred to ensure proper mixing and maintained at a constant temperature (55 °C) for a specific duration (24 h) to allow scale formation and inhibitor action. After the specified duration, the beakers were removed from the stirrer, and the formed scales were carefully collected and dried. The inhibition efficiency of the scale inhibitor was calculated by comparing the weight of the scales formed in the presence of the inhibitor with the weight of the scales formed in its absence.

2.4. Brines preparation

Laboratory analyses were conducted on brine water samples extracted from oil and gas field operations to establish the foundation of this artificially created brine. The summarized content is presented in Table 1, outlining the principal components of these brine water samples, encompassing both formation and injection waters. The table serves as a comprehensive reference for the composition of the brines, specifically delving into the cations, anions, and pertinent physical attributes. Within the formation water and injection water segments, the concentrations (expressed in mg/L) of diverse cations and anions are listed. The cataloged cations include Na^{+1}, K^{+1}, Ca^{+2}, Mg^{+2}, Sr^{+2}, and Ba^{+2}, while the anions consist of Cl^{-1}, SO_4^{-2}, and HCO_3^{-1}. It is crucial to note that there are discernible variations in the concentration levels between the formation water and injection water, with the latter exhibiting relatively lower concentrations for the majority of cations and anions. Table 2 lists the physical properties, which furnishes additional insights, encapsulating metrics like the total dissolved solids (TDS), recorded density (g/cc), pH levels, alkalinity represented by HCO_3^{-1}, and the electrical conductivity

Table 1 | Composition of brine water (formation and injection water)

Cations and anions (mg/L)	Formation water	Injection water
Na^{+1}	14,500	9,700
K^{+1}	90	55
Ca^{+2}	3,000	2,000
Mg^{+2}	215	143
Sr^{+2}	8	5
Ba^{+2}	1.5	0.9
Cl^{-}	8,000	12,000
SO_4^{-2}	5,100	3,400
HCO_3^{-1}	260	173

Table 2 | The physical properties of brine water (formation and injection water)

Total dissolved solids	42,000
Measured density	0.95
pH	7.2
Alkalinity as HCO_3^{-1}	250
Density	1.01
Electrical conductivity	0.06

(1/ohm-cm). Importantly, each of these physical attributes possesses distinct values for both formation water and injection water.

Presented in Table 3 is comprehensive data concerning the chemical composition of both synthetic formation and injection water, detailing the presence of cations, anions, and TDS. The table is distinctly divided into two segments: Formation water and Injection water. Within the Formation water and Injection water sections, the concentrations of diverse cations and anions within the synthetic water are outlined. Among the cations noted are Na^{+1}, K^{+1}, and Ca^{+2}, each exhibiting distinct concentrations for formation and injection waters. Correspondingly, the anions highlighted encompass Cl^{-1} and HCO_3^{-1}, again with different concentrations for the two types of water. The ultimate row of the table furnishes information on the TDS present in the synthetic water, offering a quantification of the collective concentration of dissolved solids in the water sample. The TDS values are presented in mg/L and exhibit variations between formation and injection waters. This tabular representation holds pivotal significance in understanding the chemical properties of synthetic formation and injection water, which hold relevance across diverse applications like the production of oil and gas, geothermal energy utilization, and environmental monitoring. By juxtaposing the data in this table with the data in the preceding table (Table 1), insights can be gained into the distinctions between natural and synthetic water, along with their potential ramifications on assorted processes.

Table 3 | The chemical composition of both synthetic formation and injection water

Cations and anions (mg/L)	Formation water	Injection water
Na^{+1}	17,892.5	12,201.75
K^{+1}	98.5	75.125
Ca^{+2}	3,347.25	2,425.75
Cl^{-1}	29,017.15	19,152.8
HCO_3^{-1}	268.7	198.6
Total Dissolved Solids (TDS)	40,204.4	28,604.25

3. RESULTS AND DISCUSSION

3.1. Characterizations

SEM was employed for the assessment of the shape and size distribution of SBA-15 and for varying loadings (5,10, and 20%) of $Cu(OH)_2$, labeled as CSBA5, CSBA10, and CSBA20, the outcomes are presented in Figure 1. The SEM micrographs in Figure 1(a) showcase the distinctive wheat-like shape of the bulk SBA-15 sample, comprising clusters of uniform rope-like aggregates. Dispersed $Cu(OH)_2$ nanoparticles are clearly visible on the surface of the mesoporous SBA-15 support, as illustrated in Figure 1(b)–1(d). Remarkably, the introduction of $Cu(OH)_2$ nanoparticles did not disturb the integrity of the SBA-15 mesostructures, a finding supported by the following XRD analysis. Some degree of aggregation of $Cu(OH)_2$ is discernible on the $Cu(OH)_2$@SBA-15 support, particularly in the case of 20% loading as observed in Figure 1(d).

An XRD analysis was conducted to unveil the phases and crystalline structures of 3D-mesoporous SBA-15 support and Copper hydroxide-loaded SBA-15 support with different ratios (5,10, and 20%), and the outcomes are illustrated in Figure 2. For XRD of SBA-15, the pattern exhibits diffraction peaks at $2\theta = 7.71°$, 22.46°, and 27.37° corresponding to a hexagonal mesoporous structure that could be indexed as (100), (110), and (200) (Lei *et al.* 2004). A broad peak centered at $2\theta = 22.46°$ is apparent, indicative of the amorphous nature of silica. The XRD pattern of as-synthesized $Cu(OH)_2$ can be primarily attributed to the orthorhombic crystalline structure $Cu(OH)_2$ (JCPDS 13-0420) (Smart *et al.* 2010). Post impregnation of $Cu(OH)_2$ onto SBA-15, in addition to the characteristic peak of SiO_2, the distinct $Cu(OH)_2$ peaks are observed and exhibit a shift toward higher values. Notably, the intensity of the SiO_2 peak diminishes with increasing loading of copper hydroxide, while the peak positions for both SBA-15 and $Cu(OH)_2$@SBA-15 remain consistent. The intensity of XRD diffraction peaks is indicative of crystallinity. As evident, the XRD diffraction peaks associated with $Cu(OH)_2$ for $Cu(OH)_2$ @SBA-15 catalysts are pronounced, suggesting high crystallinity of the prepared $Cu(OH)_2$@SBA-15 catalysts, especially for the 20% loading. This finding corroborates the widespread distribution of $Cu(OH)_2$ active species on the SBA-15 support surface. This can be attributed to the sample-specific surface area and well-developed pore structure of the SBA-15 support (as confirmed by the following N_2 adsorption–desorption analysis), providing favorable conditions for the loading of $Cu(OH)_2$ species. This suggests the preservation of the 3D-mesoporous structure of SBA-15 following the impregnation of copper hydroxide species.

Figure 3 exhibits the infrared spectra of pristine SBA-15 and copper hydroxide-loaded SBA-15 support with different ratios (5,10, and 20%). Table 4 presents the characteristic bands in the infrared spectra of pristine SBA-15 and $Cu(OH)_2$@SBA-15 nanocatalysts. The wavenumbers are associated with specific vibrational

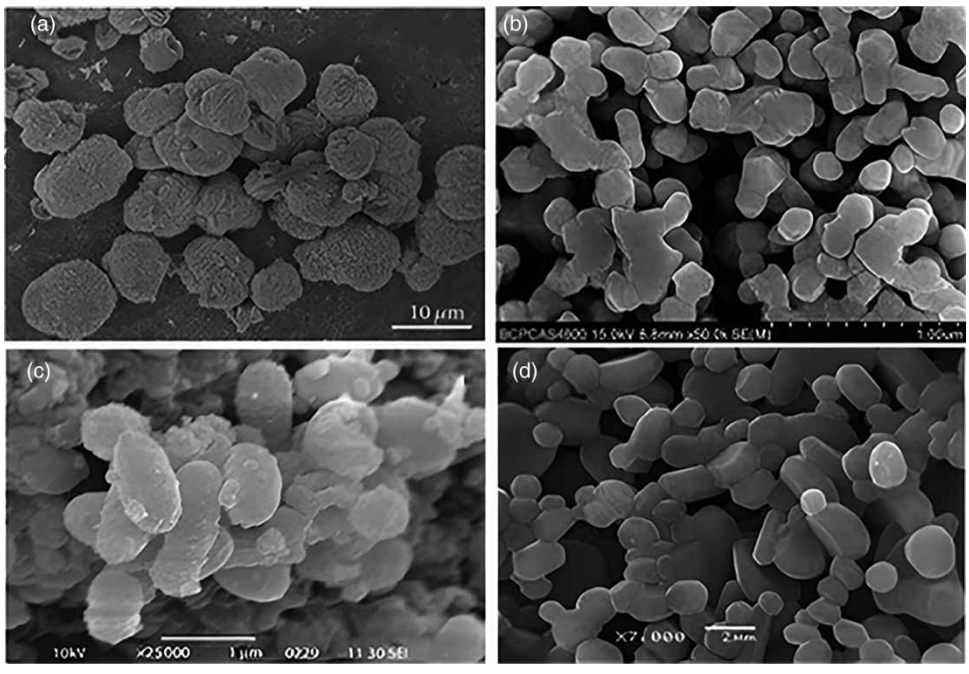

Figure 1 | SEM images of (a) SBA-15; (b) CSBA5; (c) CSBA10; and (d) CSBA20 catalyts.

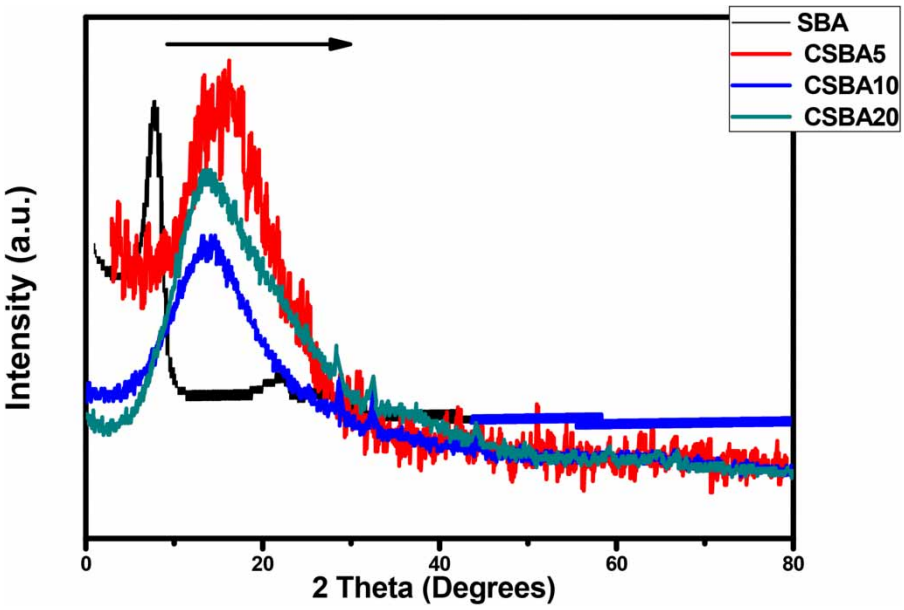

Figure 2 | XRD patterns of SBA-15; CSBA5; CSBA10; and CSBA20 catalyts.

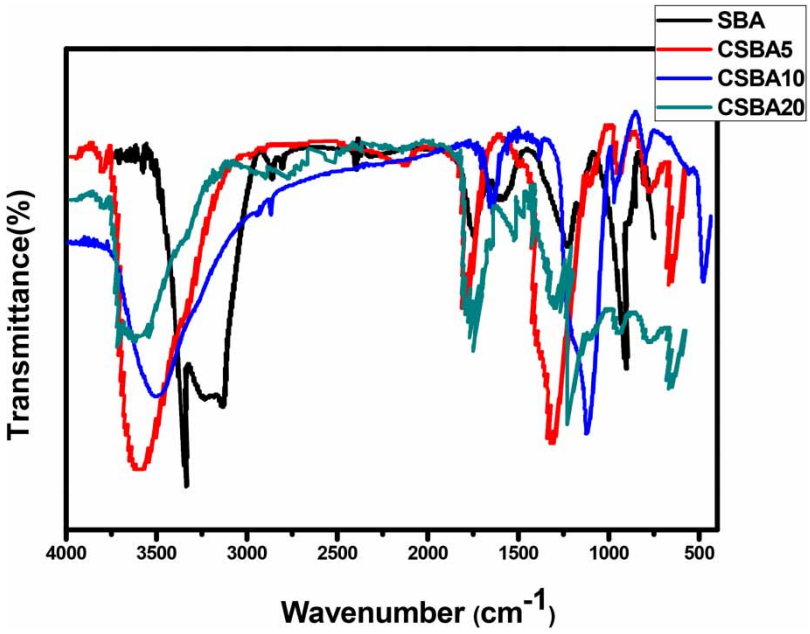

Figure 3 | Infrared spectra of SBA-15; CSBA5; CSBA10; and CSBA20 catalyts.

Table 4 | The characteristic bands in the infrared spectra of pristine SBA-15 and $Cu(OH)_2$@SBA-15 nanocatalysts

Wavenumber (cm^{-1})	Band assignment
1,085	Asymmetric stretching of Si–O–Si
805	Symmetric stretching of Si–O–Si
466	Bending vibration of Si–O–Si
950	Stretching vibration of Si–OH bond
646	Stretching vibration of C-H bond
3,650–3,200	O–H group of adsorbed water
1,630	Bending vibration of O–H in adsorbed water

modes and bond assignments. Across all samples, the distinctive bands located at 1,085, 805, and 466 cm^{-1} can be attributed to the asymmetric stretching, symmetric stretching, and bending vibration modes of Si–O–Si, respectively, arising from the underlying SBA-15 silica framework (Yao *et al.* 2018). Additionally, a subtle band at 950 cm^{-1} is indicative of the stretching vibration of the Si–OH bond (Xu *et al.* 2015). Moreover, a weak broadband around 3,650 and 3,200 cm^{-1} corresponds to the O–H group of adsorbed water on the surface of the SBA-15 mesoporous material, while the band at 1,630 cm^{-1} is assigned to the bending vibration mode of O–H in physically adsorbed water (Li *et al.* 2010; Wang *et al.* 2021). The FT-IR spectrum of CSBA reveals the existence of the bands of $Cu(OH)_2$ at 3,650, 3,200, and 940 cm^{-1} that corresponds to the stretching mode of the hydroxyl group. The band at 646 cm^{-1} is assigned to the stretching vibration of C–H (Smart *et al.* 2010). In the FT-IR spectra of $Cu(OH)_2$@SBA-15 composites, the intensity of the O–H bands notably decreases because of the interactions occurring between the surface Si–OH groups and the $Cu(OH)_2$ species.

Figure 4 represents the TGA results for the SBA-15 and those with varying loadings of $Cu(OH)_2$ catalysts. The weight loss percentages are shown at different temperature intervals. For SBA-15, an initial weight loss is observed from 0 to 170 °C (8.8%), attributed to the desorption of physically adsorbed water. Subsequently, another weight loss occurs within the temperature range of 170–800 °C (5.5%), indicative of the decomposition of the P123 template entrapped within the pores of SBA-15 (Borrajo *et al.* 2004). The $Cu(OH)_2$@SBA-15 catalysts follow a similar trend, exhibiting two main weight loss stages. The first stage, occurring within the range of 30–200 °C, corresponds to the removal of water molecules (Borrajo *et al.* 2004). The second stage, observed between 200 and 800 °C, is associated with chemically bonded water and the loss of oxygen atoms from residual metal oxides resulting from the decomposition of copper hydroxide. The weight losses for different $Cu(OH)_2$@SBA-15 loadings (5, 10, 20%) are measured at 11.6, 12.2, and 14.1%, respectively. The $Cu(OH)_2$@SBA-15 catalysts demonstrate slightly enhanced thermal stability compared with pristine SBA-15 due to factors like partial pore blockage by the copper hydroxide species or partial amorphization within the structure.

The N_2 adsorption–desorption isotherms of the synthesized SBA and $Cu(OH)_2$@SBA-15 catalysts exhibit a Type IV classification, as depicted in Figure 5. This classification points to the mesoporous nature of the prepared samples. The Type IV isotherm features a distinct capillary condensation step at higher relative pressures (around $P/P_0 = 0.55$–0.83). The presence of an H_1-type hysteresis loop in the $Cu(OH)_2$@SBA-15 catalysts can be attributed to the ordered 3D pore structure inherent to the SBA-15 material (Hoang *et al.* 2005). The hysteresis loops observed in the $Cu(OH)_2$@SBA-15 catalysts closely resemble those of pure SBA-15, suggesting that the three-dimensional mesopores of SBA-15 remain unaffected by the incorporation of copper hydroxide. However, the nitrogen adsorption–desorption curve areas related to the $Cu(OH)_2$@SBA-15 catalysts experience a reduction when compared with pure SBA-15. This implies that the introduction of copper hydroxide species results in partial blockage of SBA-15 channels and pores (Yang *et al.* 2010).

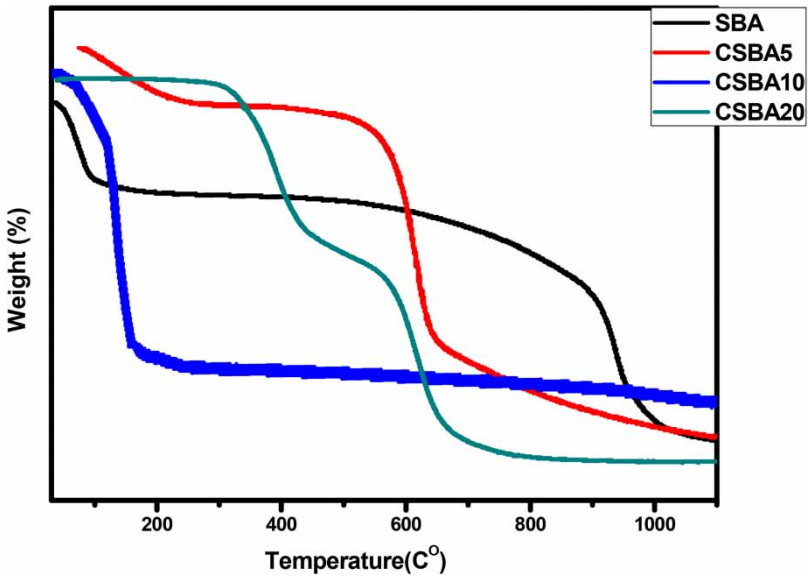

Figure 4 | Thermogravimetric analysis of SBA-15, CSBA5, CSBA10, and CSBA20 catalysts.

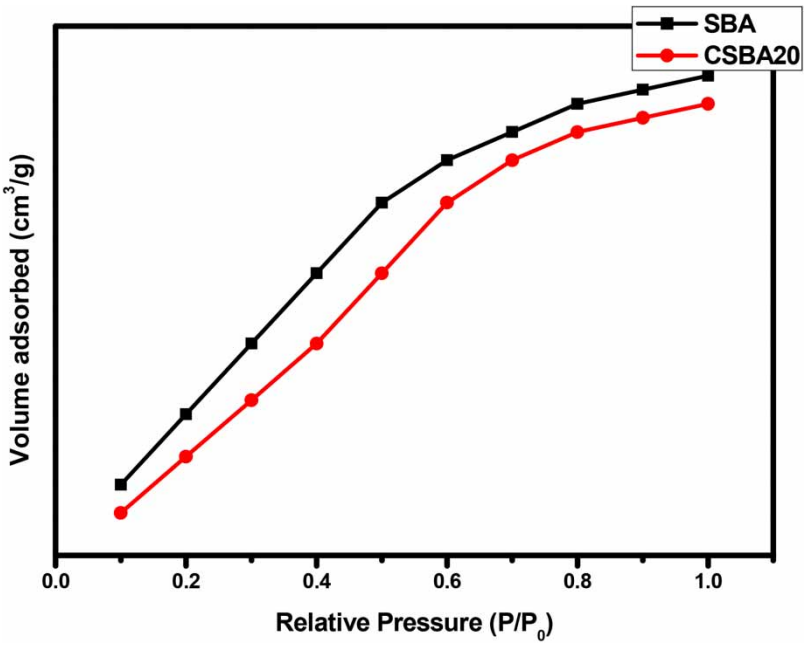

Figure 5 | N_2 adsorption–desorption isotherms of SBA and CSBA20 catalysts.

The physicochemical properties of all samples are presented in Table 5. The results provided show the specific surface area, pore size, and pore volume of different materials: SBA-15, SBA-15, CSBA5, CSBA10, and CSBA20. It is evident that the 3D-mesoporous SBA-15 boasts the highest specific surface area (918.8 m^2/g), pore size (5.33 nm), and pore volume (0.98 cm^3/g). The incorporation of copper hydroxide into the SBA-15 pore structure appears to be favorably achieved, as evidenced by the minimal expansion of the unit cell parameter and wall thickness, in comparison with the pristine SBA-15 support (refer to Table 5). Increasing the $Cu(OH)_2$ concentration to 20% leads to a significant reduction in specific surface area compared with the previous concentrations. Overall, the introduction of $Cu(OH)_2$ into the SBA-15 material leads to a decrease in specific surface area, possibly owing to the occupation of surface sites by $Cu(OH)_2$. However, the resulting materials still exhibit substantial specific surface areas and pore characteristics that make them potentially useful in various applications.

3.2. Compatibility experiments

Compatibility experiments can be conducted to determine the effectiveness of copper hydroxide-loaded SBA-15 catalysts in removing calcite scales from produced water. This information is valuable in the oil and gas industry, where the treatment and reuse of produced water for injection purposes can help minimize the use of freshwater in operations. By understanding the factors that influence the removal of calcite scales using these catalysts, operators can optimize their water treatment and injection processes to mitigate scaling issues and enhance production. Figure 6(a) presents the results of an experiment that investigated the impact of different concentrations of copper hydroxide-loaded SBA-15 catalysts on the removal of calcite scales from brine water (Ramzi *et al.* 2016). The results are depicted in mg/L for calcite scales at six different catalyst concentrations: 100, 80, 60, 40, 20, and 0%, under reservoir conditions (40 °C, 1,000 psi). It is evident that as the concentration of the

Table 5 | Physicochemical properties of catalysts

Catalyst	Specific surface area (m^2/g)	Pore size (nm)	Pore volume (cm^3/g)
SBA-15	918.8	5.33	0.98
CSBA5	764.1	5.55	1.05
CSBA10	691.7	5.75	1.12
CSBA20	564.3	6.00	1.20

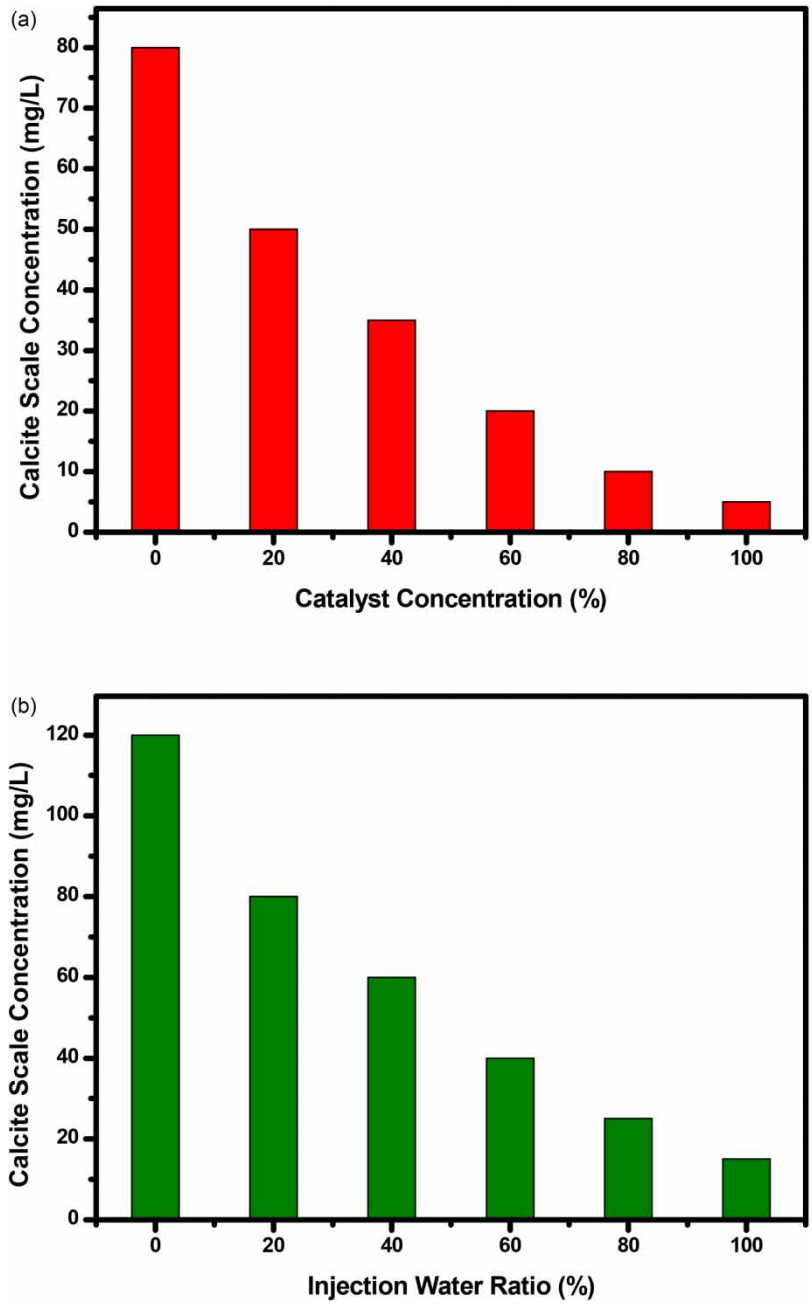

Figure 6 | (a, b) Impact of catalyst concentration and effect of injection water ratio on calcite scale removal from brine water and produced water, respectively.

catalyst decreases, the concentration of calcite scales increases. This implies an inverse relationship between the concentration of the catalyst and the concentration of calcite scales. This can be attributed to the fact that higher catalyst concentrations facilitate the more effective removal of calcite scales from the produced water. Figure 6(b) illustrates the results of an experiment that examined the effect of varying the ratio of injection water on the concentration of calcite scales in produced water when using copper hydroxide-loaded SBA-15 catalysts. The results are presented in mg/L for calcite scales at six different ratios of injection water: 100, 80, 60, 40, 20, and 0%. It can be observed that as the ratio of injection water increases, the concentration of calcite scales also increases. This indicates a direct relationship between the ratio of injection water and the concentration of calcite scales. The injection water, when mixed with the produced water, influences the pH of the produced water, which in turn affects the solubility of the calcite scales. Higher ratios of injection water can lead to changes in pH that enhance the solubility of the calcite scales, resulting in an increase in their concentration in the produced water.

The results presented in Figures 7(a) and 7(b) provide information on the scaling tendency of different substances, specifically, $CaCO_3$, $CaSO_4{\cdot}2H_2O$, and $CaSO_4$, $BaCO_3$, and $BaSO_4$ in oilfield water and synthetic water after mixing with varying percentages of injection water, as well as the ratio of injection water in synthetic samples to $CaCO_3$ scale formation. These results indicate the influence of injection water on the concentration of dissolved minerals and the pH of the mixture, which affect the scaling tendency of the substances. Figure 7(a) shows the scaling tendency of different substances in oilfield water. It is observed that as the percentage of injection water increases, the concentrations of $CaCO_3$, $CaSO_4{\cdot}2H_2O$, and $CaSO_4$, $BaCO_3$, and $BaSO_4$, decrease. This can be attributed to the fact that injection water typically has a lower concentration of dissolved minerals compared with oilfield water. When the injection water is mixed with the formation water, the concentrations of dissolved minerals in the mixture decrease, resulting in a decrease in the scale tendency of these substances. However, the scale tendency of $CaCO_3$ increases as the percentage of injection water increases. $CaCO_3$ has higher solubility at higher pH values. Since injection water usually has a higher pH than oilfield water, as the

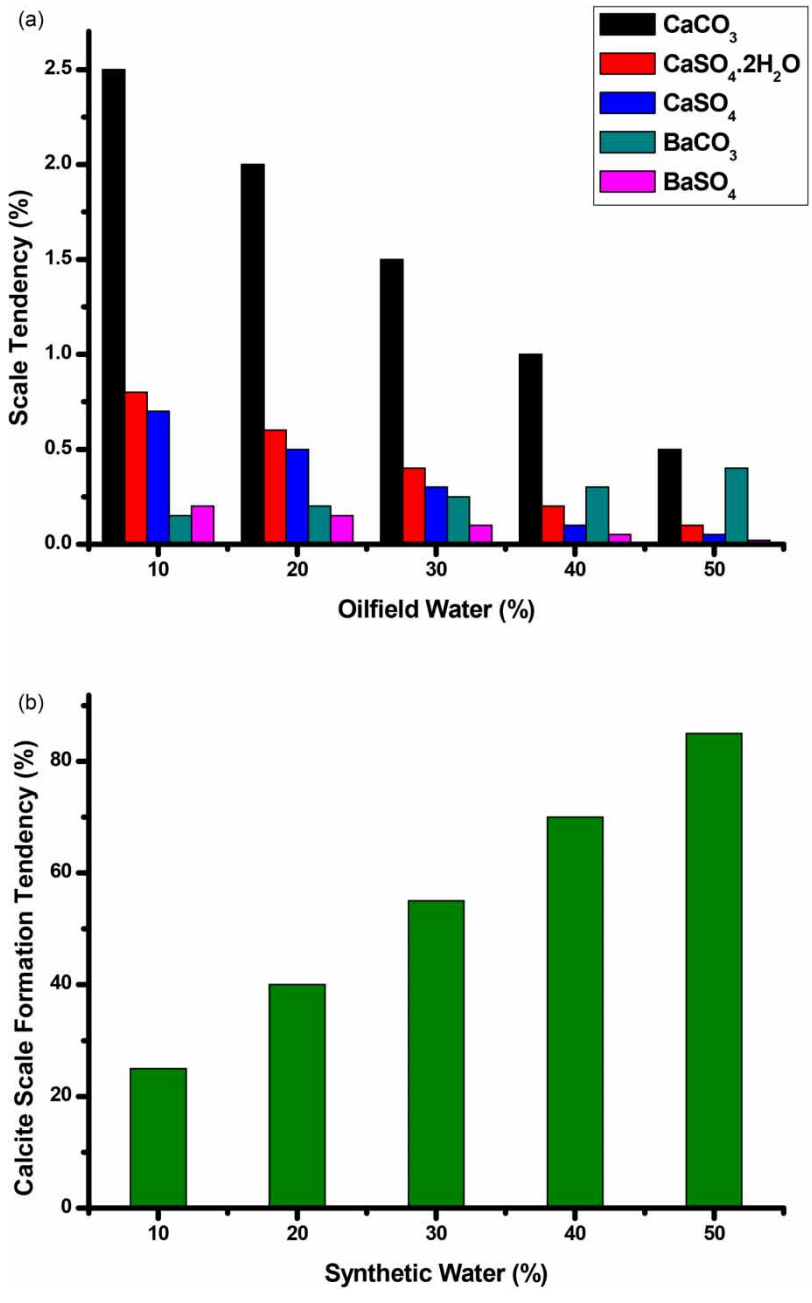

Figure 7 | Scaling tendency of the two incompatible waters: (a) oilfield water and (b) synthetic water.

percentage of injection water increases, the pH of the mixture also increases, leading to an increase in the scale tendency of $CaCO_3$.

3.3. Evaluation of the solid-scale inhibitor

The investigation into copper hydroxide-loaded SBA-15 catalysts indicates that the optimal combination of copper hydroxide and SBA-15 should be carefully determined to effectively inhibit calcite scale formation. SEM illustrates that a 20% loading of copper hydroxide on SBA-15 retains the original 3D-mesoporous structure of SBA-15, whereas higher loadings result in some degree of particle aggregation. These analyses reveal that the copper hydroxide is well-dispersed and interacts with the surface Si–OH groups of SBA-15. FT-IR spectra exhibit a reduction in the intensity of O–H bands in the CuOH@SBA-15 nanocatalysts, signifying interaction between surface Si–OH groups and copper hydroxide. From the collected data, it is evident that achieving a higher composite ratio of copper hydroxide to SBA-15, which promotes stronger interaction between the two components while minimizing aggregation, is a pivotal factor in effectively inhibiting calcite scale formation. Furthermore, the chosen ratio must strike a balance between efficient scale inhibition and the preservation of SBA-15's meso- and microporous structures. Subsequent experiments and thorough analysis are warranted to pinpoint the optimal composite ratio for this specific application. In evaluating the impact of varying temperatures on calcite scale formation during the mixing of synthetic water samples (formation water and injection water), the jar static test can be employed. Calcite scale, a prevalent inorganic scale, tends to precipitate because of the amalgamation of waters with elevated concentrations of calcium and carbonate ions.

3.3.1. Effect of pH

The impact of pH on the efficency of the copper hydroxide-loaded SBA-15 catalyst in inhibiting calcite scale formation can be assessed by examining the inhibition efficiency across various pH values. The value of pH holds significance since it influences the solubility of scale-forming minerals and the chemical interactions between the catalyst and mineral surfaces. It's crucial to recognize that the most favorable pH range for a particular catalyst is contingent upon the precise chemical composition of the scale-forming minerals and the catalyst itself. Therefore, assessing inhibition efficiency under different pH conditions becomes essential to ascertain the optimal pH range for optimal inhibition performance. Figures 8(a) and 8(b) illustrate the influence of pH on both the efficiency of the calcite scale inhibitor and the propensity for calcite scale formation. As evident from these figures, the scale inhibitor's efficiency increases while calcite scale formation decreases with a rise in pH (from 2 to 8), implying that the scale inhibitor is more potent under alkaline conditions. This phenomenon can be attributed to the heightened negative charge on the mineral surface at elevated pH levels. As a result, scale inhibitor molecules are more prone to adsorb onto the surface, enhancing inhibition performance.

In addition, pH also affects the chemical interaction between the scale inhibitor and the mineral surface, which affects the solubility of the scale-forming minerals and thus the scale inhibition performance. Therefore, evaluating the inhibition effectiveness of scale inhibitors at different pH values is a prerequisite to determining the optimal pH range to achieve the peak inhibition performance.

3.3.2. Effect of inhibitor concentration

Figure 9(a) demonstrates the impact of copper hydroxide-loaded SBA-15 catalyst concentration on the efficiency of inhibiting calcite scale formation in both oilfield water and synthetic water, as well as on calcium carbonate. The graph reveals that the inhibition effectiveness rises in correspondence with an escalation in the catalyst dosage. The inhibition rate reaches its zenith, surpassing 95%, at a critical dosage point. Beyond this point, the inhibition rate levels off, displaying a plateau or a minor reduction trend. Upon assessing the performance of calcium carbonate inhibition, a pronounced upswing of over 50% in the inhibition rate is observed as the dosage of the catalyst is augmented from 2.5 to 7.5 ppm. Optimal inhibition performance is achieved at the dosage of 7.5 ppm, showcasing an impressive inhibition efficiency of 99% on calcium carbonate. This outcome underscores the catalyst's commendable potential in inhibiting calcium carbonate scale formation. Figure 9(b) shows the effect of scale inhibitor concentrations of different scales in oilfield water and synthetic water and the $CaCO_3$ scale tendency. As the concentration of the scale inhibitor increases, the $CaCO_3$ scale tendency decreases, confirming the inhibition efficiency results. The results of both figures demonstrate the effectiveness of the scale inhibitor in inhibiting the formation of calcium carbonate scales. As the concentration of the inhibitor increases, more inhibitor molecules are available to adsorb onto the mineral surface, leading to an increase in the inhibition efficiency. At the critical dosage, the inhibition rate reaches its maximum value, indicating that the

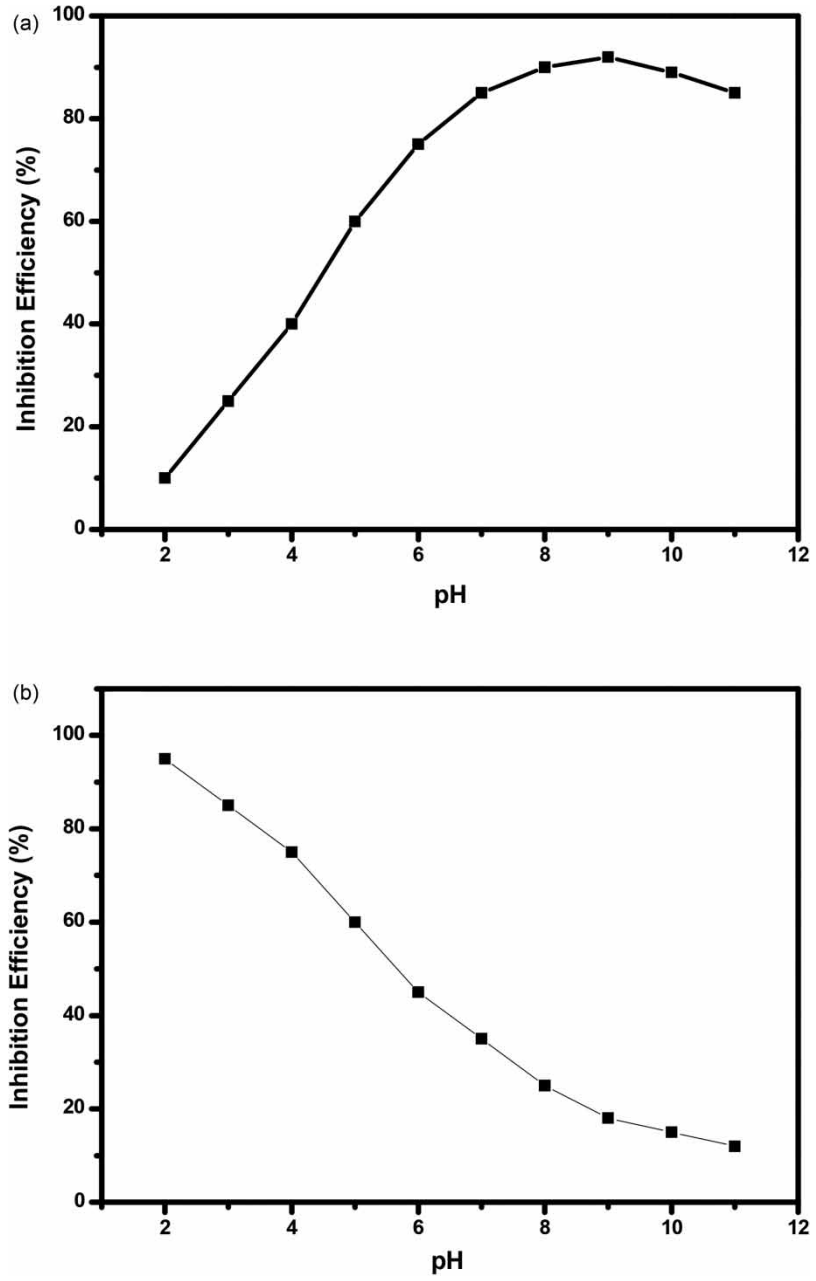

Figure 8 | The effect of pH on the performance of scale inhibitors: (a) oilfield water and (b) synthetic water.

available inhibitor molecules are sufficient to fully cover the mineral surface and prevent further scale formation. At higher concentrations, the inhibition rate may exhibit a plateau or a slight decrease tendency, which suggests that excess inhibitor molecules may not further improve the inhibition performance. The effect of the inhibitor concentration on the calcium carbonate scale tendency confirms the inhibition efficiency results, as an increase in the inhibitor concentration leads to a decrease in the scale tendency. This confirms that the inhibitor molecules are adsorbed onto the mineral surface and prevent further scale formation. This table presents the effect of scale inhibitor concentration on different scales ($BaSO_4$, $CaCO_3$, $CaSO_4{\cdot}2H_2O$) in both oilfield water and synthetic water, as well as the $CaCO_3$ scale tendency. As the concentration of the scale inhibitor increases, the scaling tendency of $CaCO_3$ decreases, aligning with the observed inhibition efficiency results. Higher inhibitor concentrations lead to more inhibitor molecules available for adsorption onto mineral surfaces, resulting in increased inhibition efficiency. At the critical dosage, the inhibition rate reaches its maximum value, indicating sufficient coverage of the mineral surface to prevent further scale formation. Higher concentrations may exhibit a

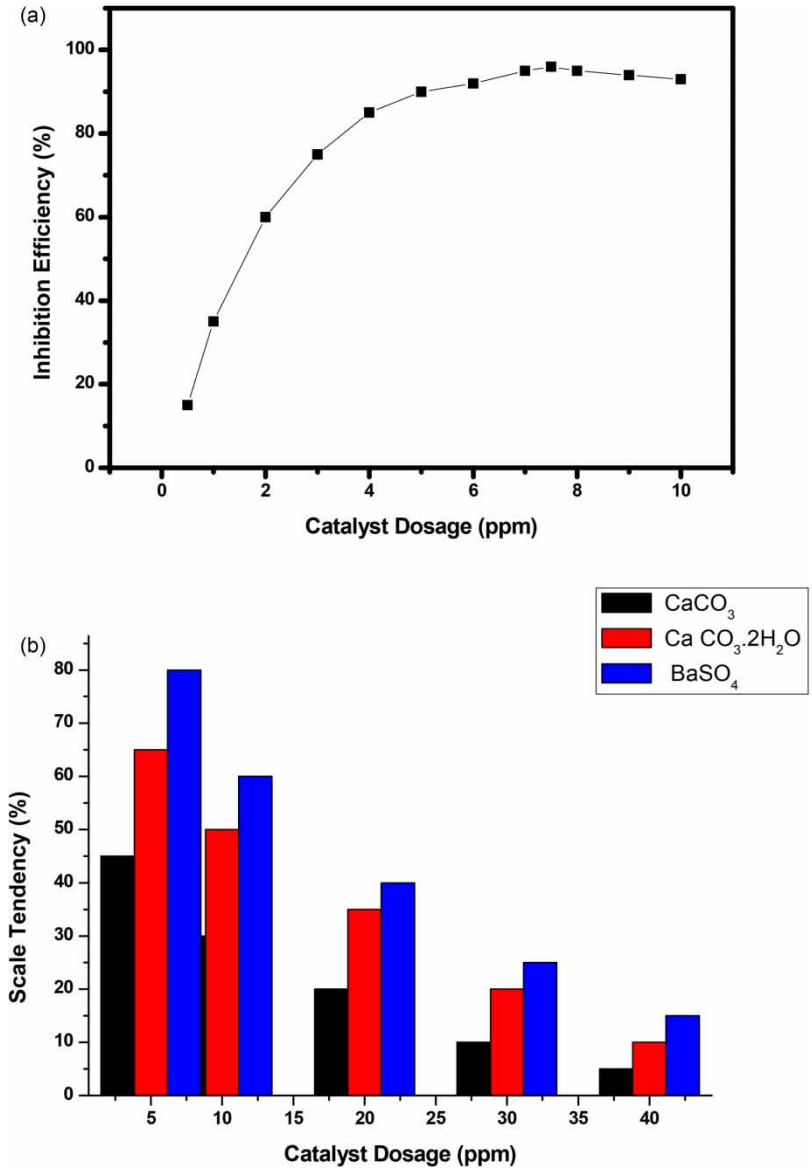

Figure 9 | Effect of scale inhibitor concentration on (a) the inhibition efficiency and (b) different scale tendencies .

plateau or slight decrease, suggesting that excess inhibitor molecules may not significantly improve inhibition performance. The decrease in $CaCO_3$ scaling tendency with increasing inhibitor concentration confirms the efficacy of inhibitor adsorption on mineral surfaces effectively preventing scale formation.

3.3.3. Effect of temperature

Figure 10 illustrates the effect of temperature on the inhibition efficiency of ionized water in oilfield water. As the temperature increases, the inhibition efficiency decreases. This is evident as the amount of scale formed increases. At lower temperatures such as 20 °C, the inhibition efficiency reaches up to 90%, and the scale formation is low. However, as the temperature rises to 95 °C, the inhibition efficiency decreases to 40%, resulting in a significant increase in the amount of scale formed. In the case of synthetic water, the inhibition efficiency remains relatively stable with increasing temperature. The amount of scale formed also remains at a moderate level across different temperatures. This is attributed to the absence of impurities in synthetic water that could interfere with the inhibition process. At 20 °C, the inhibition efficiency is 70%, and this remains relatively unchanged up to 90 °C. Overall, the results show that the inhibition efficiency of ionized water decreases with increasing temperature. However, the extent of this decrease depends on the type of water being treated. In the case of oilfield water, the inhibition efficiency decreases significantly with increasing temperature, while in the case of synthetic water, the inhibition efficiency is more stable.

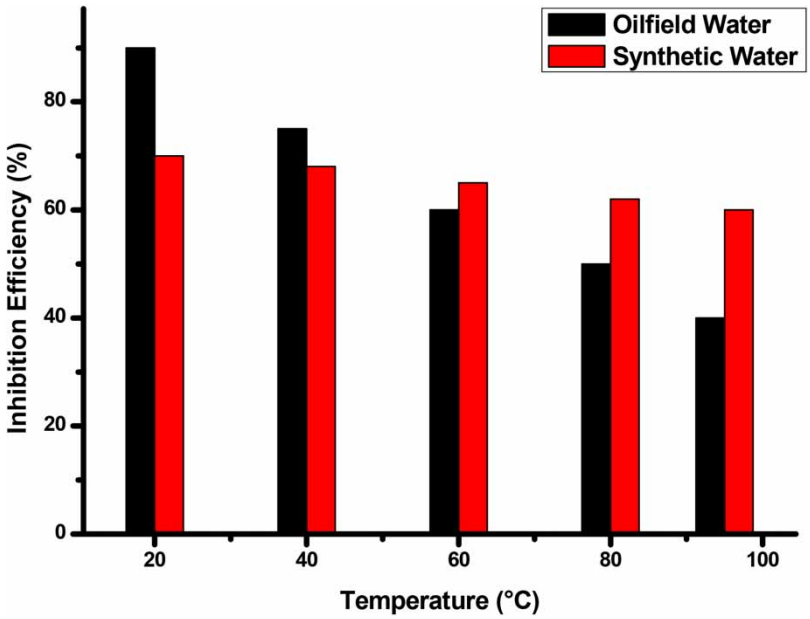

Figure 10 | Effect of temperature on inhibition efficiency in oilfield water, and synthetic water.

3.4. Mechanism of scaling control with CSBA catalyst inhibtor

The mechanism behind scale inhibition by these prepared nanoparticles is presumed to involve an adsorption process, wherein the nanoparticles adhere to the mineral crystal surfaces, thereby obstructing their growth and aggregation tendencies (Reddy & Hoch 2002). This results in the generation of smaller, more manageable crystals. Our application of CSBA nanoparticles has demonstrated their effectiveness in inhibiting crystal growth. This effectiveness is likely attributed to the distinct surface charge and adsorption characteristics of these nanoparticles, which perturb crystal growth and encourage the formation of amorphous calcium carbonate. Such an amorphous form is more readily removable compared with crystalline calcite. Considering the role of the ordered mesoporous SBA-15 support, we have found that due to its highly organized pore structure with narrow size distribution, SBA-15, also known as mesoporous silica KIT-6, exhibits considerable potential in diverse applications, including the adsorption of ions that contribute to scale formation.

3.5. Comparison of CSBA with other scale inhibitors

Table 6 provides a comparison of the efficiency of CSBA (calcite scale inhibitor) with several other calcite scale inhibitors from previous studies. The inhibitors listed in the table include AA-APEC, CM-QAOC, palm leaves extract, PASP/Cs, PAA, AA-APEC (again), CG, OAE, and CSBA (our work).

Among the inhibitors listed, CSBA demonstrates the highest inhibition efficiency at 99%. This indicates that CSBA has shown remarkable effectiveness in inhibiting the formation of calcite scale. The high inhibition

Table 6 | Comparison of CSBA efficiency with some calcite scale inhibitors of previous studies

Scale inhibitor	Inhibition effiency(%)	Ref.
AA-APEC	96%	Cao *et al.* (2014)
CM-QAOC	70.2%	Zhang *et al.* (2015)
Palm leaves extract	89.7%	Abd-El-Khalek *et al.* (2016)
PASP/Cs	92%	Zeng *et al.* (2015)
PAA	82.7%	Xue *et al.* (2012)
AA-APEC	83.6%	Xue *et al.* (2012)
CG	91%	Maher *et al.* (2020)
OAE	88	Al-Mhyawi *et al.* (2021)
CSBA	99	Our work

efficiency suggests that CSBA is a promising candidate for scale control and prevention in various industrial and domestic applications.

Comparatively, AA-APEC (96%), PASP/Cs (92%), and CG (91%) also exhibit relatively high inhibition efficiencies. These inhibitors have demonstrated good performance in inhibiting the formation of calcite scale, although they are slightly less efficient than CSBA.

CM-QAOC (70.2%) and PAA (82.7%) exhibit lower inhibition efficiencies compared with the aforementioned inhibitors. While they still provide a certain level of scale inhibition, their performance may be considered moderate in comparison.

Palm leaves extract (89.7%) and the second instance of AA-APEC (83.6%) also demonstrate respectable inhibition efficiencies, although they are lower than CSBA and some of the other inhibitors listed.

It is important to note that the references provided in the table correspond to the sources where the inhibition efficiencies of these inhibitors were reported. These references can be consulted for more detailed information on the experimental procedures and methodologies used to evaluate the inhibition efficiencies.

Overall, the comparison presented in Table 6 highlights the superior inhibition efficiency of CSBA when compared with other calcite scale inhibitors. This suggests that CSBA has the potential to be a highly effective and valuable solution in the field of scale control and prevention.

4. CONCLUSION

In the scope of this investigation, solid-scale inhibitors based on $Cu(OH)_2$-loaded SBA-15 were synthesized successfully and their scaling inhibition properties were evaluated through a static jar test. Diverse characterization techniques were employed to analyze the synthesized materials. The efficacy of these solid-scale inhibitors will be assessed using a static bottle test, with their stability examined under varying temperature and pH conditions. The outcomes of this study are anticipated to contribute to the advancement of novel and efficient solid-scale inhibitors suitable for applications within the oil and gas industry.The synthesized materials demonstrated remarkable scale inhibition properties, showcasing an inhibition efficiency of 95% for WO3-based inhibitors and 99% for $Cu(OH)_2$ nanoparticles-based inhibitors. These findings hold significant promise for the potential application of $Cu(OH)_2$-loaded SBA-15 solid-scale inhibitors as effective and sustainable solutions in addressing scaling challenges within the oil and gas industry. Notably, the scale inhibition efficiency exhibited an ascending trend, while the efficiency against calcite scale decreased with an increase in pH (ranging from 2 to 8). This suggests that the scale inhibitor exhibits enhanced performance under alkaline conditions. A notably high inhibition efficiency of 99% against calcium carbonate was achieved at an optimal dosage of 7.5 ppm, highlighting the strong inhibitory performance against calcium carbonate scaling. Furthermore, the scale inhibitor's effectiveness was observed to increase with rising temperatures, up to 55 °C. The integration of these materials could potentially lead to more efficient and cost-effective solutions for managing scaling challenges across various industrial processes.

DATA AVAILABILITY STATEMENT

All relevant data are included in the paper or its Supplementary Information.

CONFLICT OF INTEREST

The authors declare there is no conflict.

REFERENCES

Abdel-Aal, N. & Sawada, K. 2003 Inhibition of adhesion and precipitation of CaCO3 by aminopolyphosphonate. *Journal of Crystal Growth* **256** (1–2), 188–200.

Abd-El-Khalek, D., Abd-El-Nabey, B., Abdel-kawi, M. A. & Ramadan, S. 2016 Investigation of a novel environmentally friendly inhibitor for calcium carbonate scaling in cooling water. *Desalination and Water Treatment* **57** (7), 2870–2876.

Al-Mhyawi, S. R., Mubarak, M. F., Hosny, R., Amine, M., Abdelraheem, O. H., Zayed, M. A., Ragab, A. H. & El Shahawy, A. 2021 Enhanced nanofiltration process of thin film composite membrane using dodecyl phenol ethoxylate and oleic acid ethoxylate for oilfield calcite scale control. *Membranes* **11** (11), 855.

Amini, M., Naderi, R., Mahdavian, M. & Badiei, A. 2020 Effect of piperazine functionalization of mesoporous silica type SBA-15 on the loading efficiency of 2-mercaptobenzothiazole corrosion inhibitor. *Industrial & Engineering Chemistry Research* **59** (8), 3394–3404.

Amini, M., Naderi, R., Mahdavian, M. & Badiei, A. 2021 Release of lanthanum cations loaded into piperazine-modified SBA-15 to inhibit the mild steel corrosion. *Microporous and Mesoporous Materials* **315**, 110908.

Bader, M. 2007 Sulfate removal technologies for oil fields seawater injection operations. *Journal of Petroleum Science and Engineering* **55** (1–2), 93–110.

Baker, D. 1999 *Development of Scaling Prediction Tools for Solar hot Water Systems. Part B-Development of an Improved Calcium Carbonate Scaling Rate Model-An Experimental and Analytical Investigation*. The University of Texas at Austin, Austin, TX, US.

BinMerdhah, A. B. 2012 Inhibition of barium sulfate scale at high-barium formation water. *Journal of Petroleum Science and Engineering* **90**, 124–130.

Borrajo, J. P., Liste, S., Serra, J., González, P., Chiussi, S., León, B., Pérez Amor, M., Ylänen, H. O. & Hupa, M. 2004 Influence of the network modifier content on the bioactivity of silicate glasses. *Key Engineering Materials* **254**, 23–26.

Cao, K., Huang, J., Zhou, Y., Liu, G., Wang, H., Yao, Q., Liu, Y., Sun, W. & Wu, W. 2014 A multicarboxyl antiscalant for calcium phosphate and calcium carbonate deposits in cooling water systems. *Desalination and Water Treatment* **52** (37–39), 7258–7264.

Coday, B. D., Xu, P., Beaudry, E. G., Herron, J., Lampi, K., Hancock, N. T. & Cath, T. Y. 2014 The sweet spot of forward osmosis: Treatment of produced water, drilling wastewater, and other complex and difficult liquid streams. *Desalination* **333** (1), 23–35.

Crabtree, M., Eslinger, D., Fletcher, P., Miller, M., Johnson, A. & King, G. 1999 Fighting scale: Removal and prevention. *Oilfield Review* **11** (03), 30–45.

Diab, M., Shreteh, K., Volokh, M. & Mokari, T. 2021 Formation of copper oxide nanotextures on porous calcium carbonate templates for water treatment. *Molecules* **26** (19), 6067.

Fakhru'l-Razi, A., Pendashteh, A., Abdullah, L. C., Biak, D. R. A., Madaeni, S. S. & Abidin, Z. Z. 2009 Review of technologies for oil and gas produced water treatment. *Journal of Hazardous Materials* **170** (2–3), 530–551.

He, S., Kan, A. T. & Tomson, M. B. 1999 Inhibition of calcium carbonate precipitation in NaCl brines from 25 to 90 C. *Applied Geochemistry* **14** (1), 17–25.

Hoang, V.-T., Huang, Q., Eić, M., Do, T.-O. & Kaliaguine, S. 2005 Structure and diffusion characterization of SBA-15 materials. *Langmuir* **21** (5), 2051–2057.

Hosny, R., Amine, M., Fathy, M. & Ramzi, M. 2019 Investigation of the impact of scale inhibitors: ethoxylated 1-Octanol and methylcyclohexanol for scale deposition control in oilfield. *Petroleum & Petrochemical Engineering Journal* **3** (2), 1–11.

Hosny, R., Desouky, S., Ramzi, M., Abdel-Moghny, T., El-Dars, F. & Farag, A. 2007 Novel scalechem programe for monitoring and enhancing dissolution of scale deposits near wellbore. *Material Science Research of India* **4** (2), 251–261.

Hosny, R., Desouky, S., Ramzi, M., Abdel-Moghny, T., El-Dars, F. & Farag, A. 2009 Estimation of the scale deposits near wellbore via software in the presence of inhibitors. *Journal of Dispersion Science and Technology* **30** (2), 204–212.

Jordan, M., Graff, C. & Cooper, K. 2001 Deployment of a scale squeeze enhancer and oil-soluble scale inhibitor to avoid oil production losses in low water-cut well. *SPE Production & Facilities* **16** (04), 267–276.

Kassab, M. A., Abbas, A. E., Elgamal, I., Shawky, B. M., Mubarak, M. F. & Hosny, R. 2021 Review on the estimating the effective way for managing the produced water: Case study. *Open Journal of Modern Hydrology* **11** (2), 19–37.

Le, H. V., Ho, K. V., Le, T. T., Nguyen, V. T., Le, H. X. & Nguyen, K. D. 2021 Synthesis and application of SBA-15-supported CuO as an efficient catalyst for the oxidative C (sp2)-O coupling reaction. In *IOP Conference Series: Earth and Environmental Science*. IOP Publishing.

Lei, J., Fan, J., Yu, C., Zhang, L., Jiang, S., Tu, B. & Zhao, D. 2004 Immobilization of enzymes in mesoporous materials: Controlling the entrance to nanospace. *Microporous and Mesoporous Materials* **73** (3), 121–128.

Li, Q., Zhang, L., Zhang, Z., Zhou, N., Cheng, Z. & Zhu, X. 2010 Air-tolerantly surface-initiated AGET ATRP mediated by iron catalyst from silica nanoparticles. *Journal of Polymer Science Part A: Polymer Chemistry* **48** (9), 2006–2015.

Lytle, D. A., Wahman, D. G., Schock, M. R., Nadagouda, M. N., Harmon, S., Webster, K. & Botkins, J. 2019 Georgeite: A rare copper mineral with important drinking water implications. *Chemical Engineering Journal* **355**, 1–10.

Maher, Y. A., Ali, M. E., Salama, H. E. & Sabaa, M. W. 2020 Preparation, characterization and evaluation of chitosan biguanidine hydrochloride as a novel antiscalant during membrane desalination process. *Arabian Journal of Chemistry* **13** (1), 2964–2981.

Merdhah, A. B. B. & Yassin, A. A. M. 2007 Scale formation in oil reservoir during water injection at high-salinity formation water. *Journal of Applied Sciences* **7** (21), 3198–3207.

Moghadasi, J., Jamialahmadi, M., Müller-Steinhagen, H. & Sharif, A. 2004 Formation damage due to scale formation in porous media resulting from water injection. In: *SPE International Conference and Exhibition on Formation Damage Control*. SPE.

Nasiri, M. & Jafari, I. 2017 Produced water from oil-gas plants: A short review on challenges and opportunities. *Periodica Polytechnica Chemical Engineering* **61** (2), 73–81.

Neville, A. & Morizot, A. 2000 A combined bulk chemistry/electrochemical approach to study the precipitation, deposition and inhibition of CaCO3. *Chemical Engineering Science* **55** (20), 4737–4743.

Ramzi, M., Hosny, R., El-Sayed, M., Fathy, M. & Abdel Moghny, T. H. 2016 Evaluation of scale inhibitors performance under simulated flowing field conditions using dynamic tube blocking test. *Int. J. Chem. Sci.* **14** (1), 16–28.

Reddy, M. M. & Hoch, A. R. 2002 Calcite crystal growth rate inhibition by aquatic humic substances. In: *Advances in Crystal Growth Inhibition Technologies* (Amjad, Z., ed.). Springer, Cham, pp. 107–121.

Smart, S., Lin, C., Ding, L., Thambimuthu, K. & Da Costa, J. D. 2010 Ceramic membranes for gas processing in coal gasification. *Energy & Environmental Science* **3** (3), 268–278.

Wang, S., Zhang, Q., Cui, C., Niu, H., Wu, C. & Wang, J. 2021 Ionic liquids-SBA-15 hybrid catalysts for highly efficient and solvent-free synthesis of diphenyl carbonate. *Green Energy & Environment* **8** (1), 183–193.

Xu, H., Zhao, H., Song, H., Miao, Z., Yang, J., Zhao, J., Liang, N. & Chou, L. 2015 Functionalized ionic liquids supported on silica as mild and effective heterogeneous catalysts for dehydration of biomass to furan derivatives. *Journal of Molecular Catalysis A: Chemical* **410**, 235–241.

Xue, X., Fu, C., Li, N., Zheng, F., Yang, W. & Yang, X. 2012 Performance of a non-phosphorus antiscalant on inhibition of calcium-sulfate precipitation. *Water Science and Technology* **66** (1), 193–200.

Yang, Y., Guan, J., Qiu, P. & Kan, Q. 2010 Enhanced catalytic performances by surface silylation of Cu (II) schiff base-containing SBA-15 in epoxidation of styrene with H2O2. *Applied Surface Science* **256** (10), 3346–3351.

Yao, N., Lu, M., Liu, X. B., Tan, J. & Hu, Y. L. 2018 Copper-doped mesoporous silica supported dual acidic ionic liquid as an efficient and cooperative reusability catalyst for Biginelli reaction. *Journal of Molecular Liquids* **262**, 328–335.

Zeng, D., Chen, T. & Zhou, S. 2015 Synthesis of polyaspartic acid/chitosan graft copolymer and evaluation of its scale inhibition and corrosion inhibition performance. *International Journal of Electrochemical Science* **10** (11), 9513–9527.

Zhang, H., Cai, Z., Jin, X., Sun, D., Wang, D., Yang, T., Zhang, J. & Han, X. 2015 Preparation of modified oligochitosan and evaluation of its scale inhibition and fluorescence properties. *Journal of Applied Polymer Science* **132** (37), 1–11.

First received 30 July 2023; accepted in revised form 11 October 2023. Available online 30 December 2023